Ionic Conductivity of a Single Porous MnO_2 Mesorod at Controlled Oxidation States

Timothy Plett,[a] Trevor Gamble,[a] Eleanor Gillette,[b] Sang Bok Lee,[b] and Zuzanna S. Siwy[a,c]
[a] *Department of Physics, University of California, Irvine, Irvine, CA 92697-4575 USA.*
[b] *Department of Chemistry and Biochemistry, University of Maryland, College Park, Maryland 20742, USA.*
[c] *Department of Chemistry, University of California, Irvine, Irvine, CA 92697-2025 USA.*

Included: Full Derivation of Gold Scattering into Nanopore; Experimental Apparatus; SEM images of mesorods; CVs demonstrating reversibility of deposited MnO_2; I-V curves for (a) a multipore sample, (b) comparison before and after gold deposition (c) two additional single mesorod/pore samples; a set of reversal potential data; saturation data for a 100nm nanorod/pore

1. Gold Scattering into a Nanopore

Considering that sputtering deposits thin films by relying on scattered atoms, a mathematical model can be devised based on solid angle scattering into a cylinder. A simplified two-dimensional model based on azimuthal scattering cannot be used because it assumes a full range of lateral scattering (Θ_s), which is clearly limited by pore width. By lateral scattering, we mean the full range of polar angles in the plane defined by an axis through the azimuthal angle and the horizontal axis (Fig. S1). What follows from this is an involved, but numerically solvable, geometry problem, visualized in Figure S2.a. An efficient way to use the model is to solve for film thickness at a given depth, d, inside the nanopore (radius, r). For chosen d and given r, we may calculate an angle, $\theta_{z\max}$, which dictates the maximum range of azimuthal scattering:

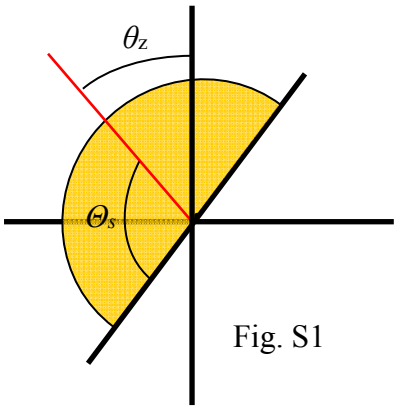

Fig. S1: A pictorial representation of azimuthal and lateral scattering angles

$$\theta_{z\max} = \tan^{-1}\left(\frac{2r}{d}\right) \qquad (S1)$$

However, exploring the range of azimuthal angles, θ_z, we identify a variety of lateral scattering angles, θ_s, dependent on θ_z (also visualized in Fig. S2.a by three triangles). Since θ_s is dependent on θ_z, we may propose a general equation ($S2$) to solve for film thickness at a given depth, λ_d:

$$\lambda_d = \lambda_o \frac{\theta_{z\max}}{\pi} \int_0^{\theta_{z\max}} \Theta_S(\theta_z) d\theta_z \qquad (S2)$$

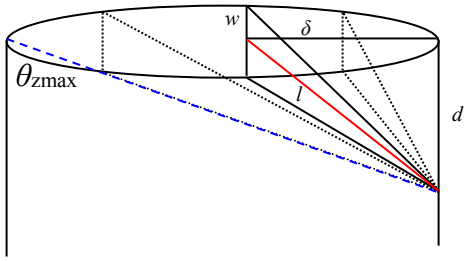

Fig. S2.a

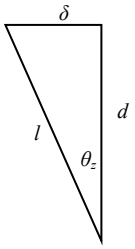

Fig. S2.b

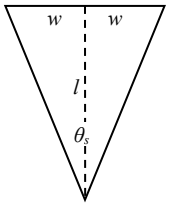

Fig. S2.c

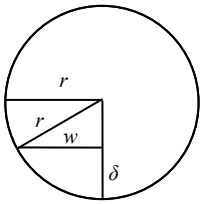

Fig. S2.d

Figure S2.a Scheme of the geometry that comes out of assuming a three-dimensional scattering. The scheme indicates how lateral scattering angle, θ_s, into the cylinder increases, then decreases, in accordance with the pore geometry. **Figures S2.b, c, d** further define variables in the geometry which is useful in framing and solving Equation (S2).

The expression, $\Theta_S(\theta_z)$, represents the equation for lateral scattering angle based on azimuthal scattering angle, θ_z. But since θ_z is itself dependent on d and r, the equation must be determined based on these two known factors. Figures S2.b-d depict the necessary geometric steps for clearly framing the desired equation. From this, we can accurately define radial entry point, δ, and scattering path, l, in terms of θ_z, as well as define width, w, in terms of δ and r:

$$\delta = \tan(\theta_z) d, \quad l = \frac{d}{\cos(\theta_z)}, \quad w = \sqrt{r^2 - (r-\delta)^2} = \sqrt{2r\delta - \delta^2} \qquad (S3)$$

By substitution, we can now frame $\Theta_S(\theta_z)$:

$$\theta_s = 2\tan^{-1}\left(\frac{w}{l}\right) = 2\tan^{-1}\left(\frac{\sqrt{2r\delta-\delta^2}\cos(\theta_z)}{d}\right) = 2\tan^{-1}\left(\frac{\sqrt{(2r - d\tan(\theta_z))\, d\tan(\theta_z)}\cos(\theta_z)}{d}\right) \qquad (S4)$$

Despite the deterministic geometry of the problem, the final expression is virtually impossible to solve analytically. However, a numerical solution is easily obtained by summation:

$$\lambda_d = \lambda_o \frac{\Delta}{\pi} \sum_{\theta_z=0}^{\theta_{z\max}} 2\tan^{-1}\left(\frac{\sqrt{(2r - d\tan(\theta_z))\, d\tan(\theta_z)}\cos(\theta_z)}{d}\right) \Big/ \pi \qquad (S5)$$

Δ represents the angle increment used in the summation, e.g. $\pi/360$, and we divide by π for both lateral and azimuthal scattering because we assume a homogeneous distribution of scattering angles for the free metal atoms in both the sputtering and evaporation deposition methods. We

used Mathematica to perform this calculation at an angle increment of $\pi/10000$ for a variety of radial-length depths. What we found was an attenuating thickness. At $d = r/2$, homogeneous scattering yielded a result $\lambda_d = .19966\lambda_o$. A more complete treatment of results is shown below in Table S1.

depth, d	λ_d/λ_o, $\theta_l = \pi$	λ_d/λ_o $\theta_l = 2\pi/3$	λ_d/λ_o $\theta_l = \pi/2$
$r/2$	0.19966	0.2995	0.3993
r	0.1205	0.18075	0.2410
$3r/2$	0.0784	0.1176	0.1568
$2r$	0.05387	0.0808	0.10774

Table S1. Simulated relative Au film thickness at different depths, d, of a pore with opening diameter of 200 nm (r = 100 nm). The values were obtained from eq. ($S5$). Figure 1 in the main manuscript plots λ_d/λ_o as a function of d. Different scenarios of homogeneous lateral scattering are considered in an attempt to account for how the width of the deposition chamber could affect particle scattering.

Experimental Apparatus

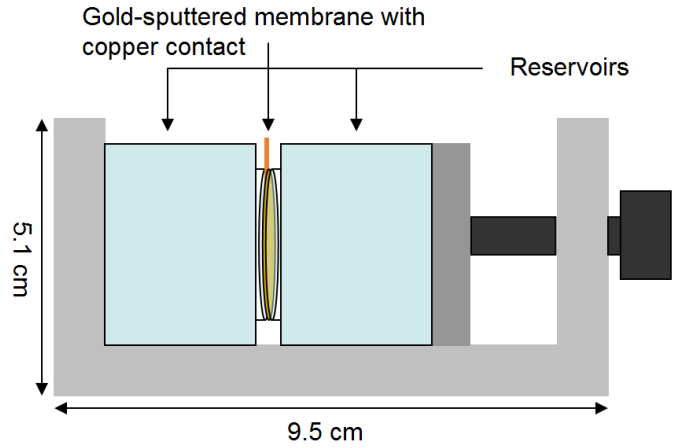

Figure S3 Scheme of the conductivity cell used in the reported experiments. The MnO_2 rod would be electrodeposited on the side of the membrane facing the left reservoir, with the gold sputtered membrane in contact with a wick of copper tape, which would connect to the working electrode during the lithiation and delithiation processes, as shown in the main text.

SEM Images of MnO_2 Mesorods Grown from 50nm Au Films

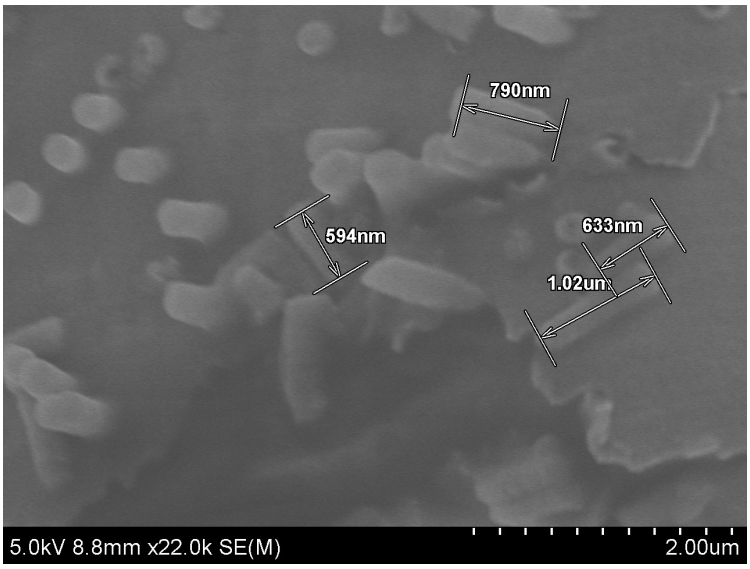

Figure S4. SEM images taken after the MnO_2 electrodeposition process was attempted on a commercial Whatman multipore (10^8/cm) film, which had been sputter coated with a 50nm thick layer of gold. The image demonstrates viability of growing mesorods using the thin gold film technique proposed earlier.

Multipore Experiments Demonstrating Reversibility and Proof of Concept

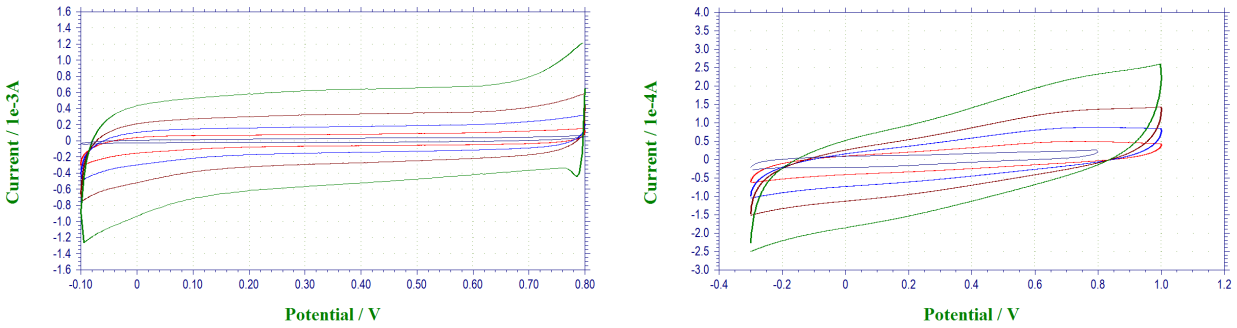

Figure S5. CVs demonstrating electrochemical reversibility in (left) 100mM $LiClO_4$ aqueous solution and (right) 100mM $LiClO_4$ propylene carbonate solution at scan rates of 100mV/s, 50mV/s, 25mV/s, and 10mV/s. The smallest scan on both CVs is the gold-sputtered multipore membrane's response to a 100mV/s sweep in the respective solutions. This is to demonstrate the change in capacitance resulting from the deposition of amorphous MnO_2 mesorods. The voltage window was restricted (-0.1 – 0.8V) in aqueous solution in an attempt to avoid excessive H_2 or O_2 evolution. The voltage window in the organic solution was widened (-0.3 – 1V) to demonstrate reversibility in the regimes used for lithiation (-0.22V) and delithiation (+1V). The voltage window for the membrane response in PC was reduced (-0.3–0.8V) to clearly distinguish it from other scans. All CVs were taken against a reference of Ag/AgCl in 3M KCl, using a CH Instruments 650C Electrochemical Analyzer and related software as a three-probe potentiostat.

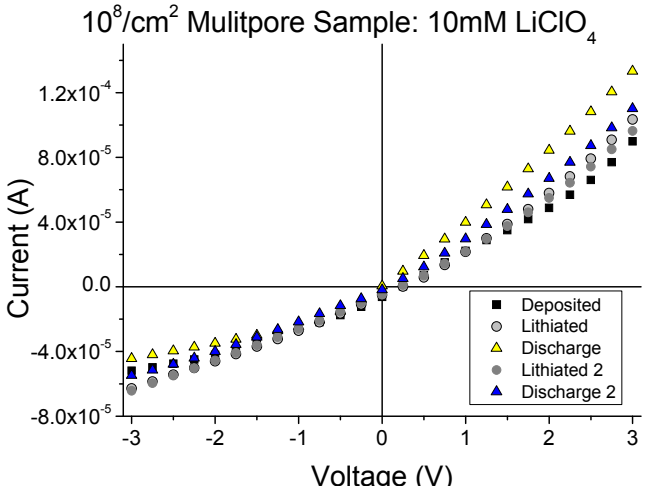

Figure S6. Current-voltage curves through a Whatman multipore polycarbonate membrane with 200 nm in diameter pores and electrodeposited MnO_2. The deposition occurred after sputtering of 50 nm thick gold. $LiClO_4$ in propylene carbonate was used as an electrolyte in order to minimize hydrogen ion intercalation in the MnO_2 rods. Despite the different electrolyte, rectification was still observed, following the same pattern described in the single nanorod case (see the main text).

Additional Single Nanopore and Nanorod/Pore System Experiments

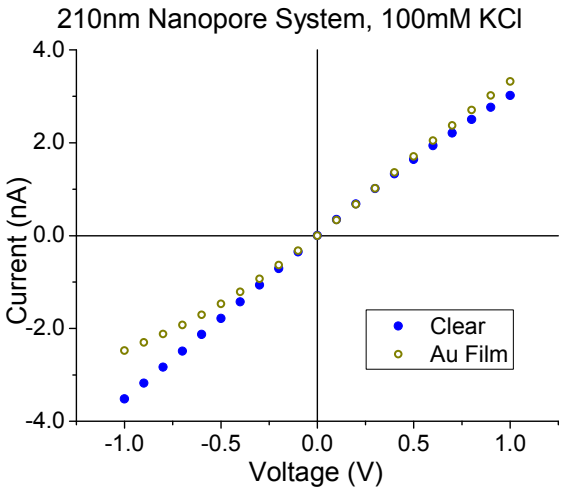

Figure S7. Current-voltage curves through a single pore with an opening diameter of 210 nm before and after sputtering of 50 nm thick gold. The recordings were performed in 100 mM KCl.

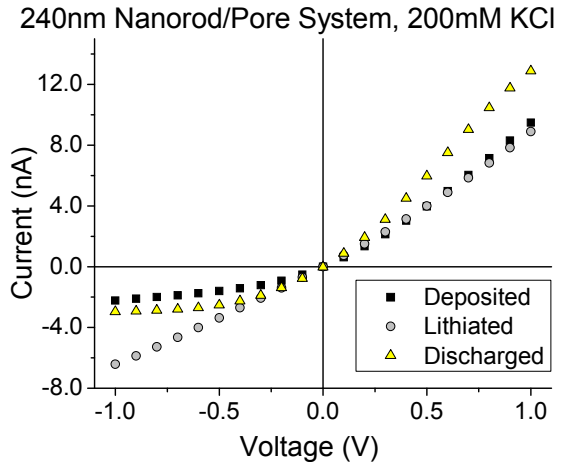

Figure S8. Current-voltage curves through a single pore with an opening diameter of 240 nm and electrodeposited MnO_2 rod. Lithiation and de-lithiation processes were performed in $LiClO_4$ in propylene carbonate, at -0.22V and 0.6V vs. Ag/AgCl (3M) respectively; current-voltage curves were recorded in an aqueous solution in KCl (200 mM).

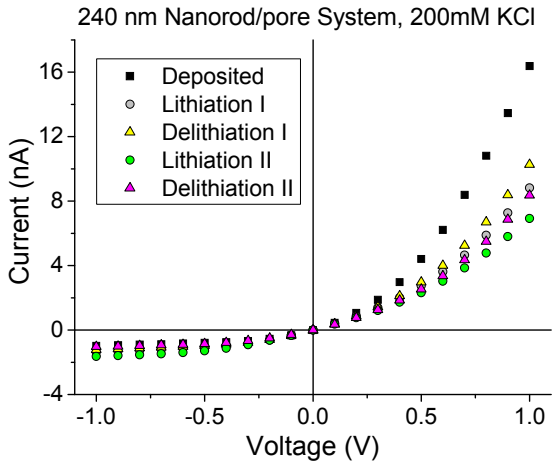

Figure S9. Current-voltage curves through a single pore with an opening diameter of 240 nm and electrodeposited MnO_2 rod. Lithiation and de-lithiation processes were performed in $LiClO_4$ in propylene carbonate; current-voltage curves were recorded in an aqueous solution in KCl. This figure demonstrates the viability of cycling a single MnO_2 rod system.

Tables S2 and S3 of reversal potential measurements, see Figure 6 of the main text for electrode arrangement on side 1 and side 2 of the membrane.

Table S2

(S)1 / (S)2	Deposit	Lith	Delith
100 mM / 10 mM	+22mV	+14mV	+12mV
10 mM / 100 mM	-12mV	-9mV	-9mV

Table S3

(S)1 / (S)2	Deposit	Lith I	Delith I	Lith II	Delith II
100 mM / 10 mM	+55mV	+17mV	+17mV	+15mV	+22mV
10 mM / 100 mM	-48mV	-14mV	-11mV	-11mV	-16mV

Tables S2 & S3. Reversal potential measurements for the 325nm mesorod/pore system (**S2**) described in Fig. 2 of the main text and (**S3**) a 180nm mesorod/pore system. We observe initial deposition of the mesorod has a higher reversal potential, which is reduced following lithiation. As with the sample presented in the main text, subsequent delithiation does not generate significant difference in response at these concentrations.

Ion Current Saturation in 130nm Nanorod/Pore System

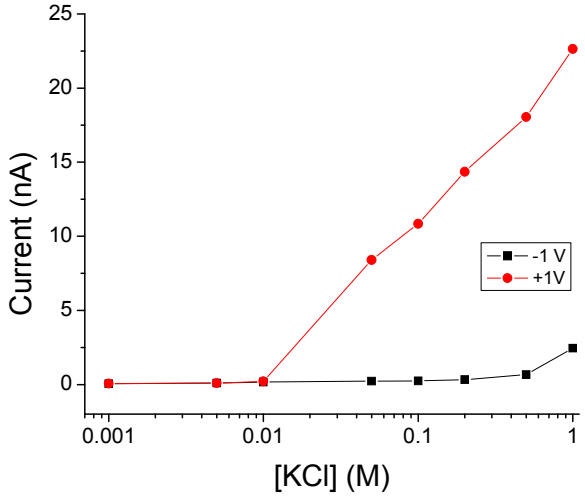

Figure S10. Ionic current recordings at ±1V bias for a 130nm pore/rod system. The system exhibited significant rectification as explained in the main text. Saturation of ion currents for both voltage biases becomes very apparent at 10mM as evidenced by the severe drop in ionic current. This set of data shows that the concentration at which the ion current saturation occurs is not dependent on the diameter of the nanopore template used for MnO_2 deposition.